

# Acoustic force spectroscopy

Gerrit Sitters<sup>1,2,4</sup>, Douwe Kamsma<sup>1,2,4</sup>,  
Gregor Thalhammer<sup>3</sup>, Monika Ritsch-Marte<sup>3</sup>,  
Erwin J G Peterman<sup>1,2,5</sup> & Gijs J L Wuite<sup>1,2,5</sup>

**Force spectroscopy has become an indispensable tool to unravel the structural and mechanochemical properties of biomolecules. Here we extend the force spectroscopy toolbox with an acoustic manipulation device that can exert forces from subpiconewtons to hundreds of piconewtons on thousands of biomolecules in parallel, with submillisecond response time and inherent stability. This method can be readily integrated in lab-on-a-chip devices, allowing for cost-effective and massively parallel applications.**

Single-molecule experiments have revolutionized the study of biomolecules, allowing scientists to perform techniques, such as force-induced denaturation, that were hitherto impossible<sup>1–3</sup>. So far, single-molecule instruments using magnetic forces (magnetic tweezers), mechanical forces (atomic force microscopy) and radiation pressure (optical tweezers) have remained rather complex, requiring specialized expertise for construction and operation and restricting their use mainly to specialized biophysics labs. In addition, most single-molecule techniques allow the user to study only a limited number of biomolecules (often one) simultaneously, thereby lowering experimental throughput and limiting statistics<sup>2,4</sup>. On the single-molecule level, discriminating heterogeneous behavior and rare events from intrinsic stochasticity requires many independent measurements<sup>2,5</sup>. Novel methods that are simpler and more cost-effective, have a smaller footprint and allow high throughput are desirable<sup>6–8</sup>.

Here we present a single-molecule manipulation method, acoustic force spectroscopy (AFS), that uses acoustic forces to stretch multiple molecules individually tethered between a surface and a microsphere. We demonstrate that AFS allows the application of controlled forces of up to 120 pN or higher—strong enough to induce major conformational changes such as DNA overstretching and mechanical unfolding of proteins<sup>1,9,10</sup>—in a highly parallel fashion.

In our AFS instrument (**Fig. 1a,b**) we used a piezo element driven by an oscillating voltage to resonantly excite a planar acoustic standing wave over a flow cell. A microsphere (with

volume  $V$ ) subjected to this standing wave experiences a force  $F$  along the vertical ( $z$ ) direction

$$F = -V\nabla \left[ \frac{1-\kappa^*}{4} \kappa_m p^2 - \frac{(\rho^* - 1)}{2\rho^* + 1} \rho_m v^2 \right] \quad (1)$$

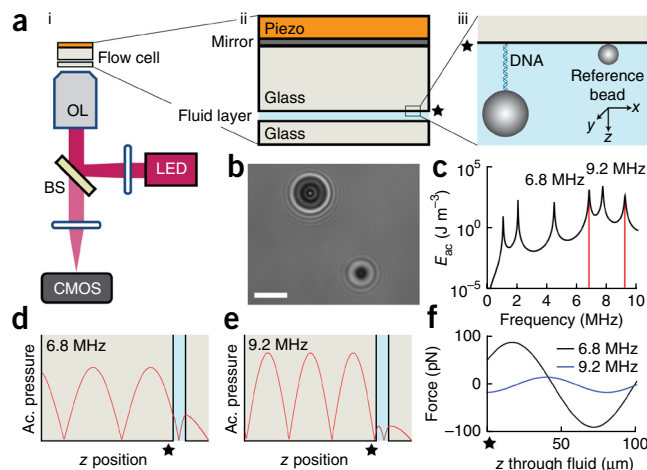
in which  $p$  is the acoustic pressure,  $v$  the acoustic velocity, and  $\rho^*$  ( $=\rho_p/\rho_m$ ) and  $\kappa^*$  ( $=\kappa_p/\kappa_m$ ) are the density ratio and compressibility ratio between the particle and the medium, respectively<sup>11</sup>. In the case of polystyrene or silica microspheres in water, the force is dominated by the gradient of the squared acoustic pressure, driving the microspheres toward an acoustic pressure node.

We calculated resonance frequencies and force profiles of the flow chamber (originally designed for an instrument combining optical tweezers and microfluidics<sup>12</sup>) using a one-dimensional model (Online Methods)<sup>13</sup> and compared them to experimentally obtained values. Driving the piezo element at a predicted frequency of 6.8 MHz (measured at 6.7 MHz, determined from the maximum force obtained with a frequency sweep; see below) resulted in a strong pull away from the surface for microspheres near the upper glass-water interface (**Fig. 1c,d,f**). We used this force to apply tension to biomolecules tethered between the upper surface and the microsphere. The force was constant within 5% when the microsphere's axial position was changed by 1  $\mu\text{m}$ , which was the length scale of the force-induced extension of the biomolecules used here. Another predicted resonance at 9.2 MHz (measured at 9.0 MHz) pushed microspheres toward the surface, which was useful because it allowed precise determination of the surface location and in principle could facilitate interactions between functionalized microspheres and surface-attached biomolecules (**Fig. 1c,e,f**).

We determined microsphere positions by analyzing the images obtained with a 40 $\times$  air-spaced objective (numerical aperture (NA) = 0.75) and a digital camera (**Fig. 1a,b**). Our tracking software (freely available at [http://figshare.com/articles/AFS\\_software/1195874](http://figshare.com/articles/AFS_software/1195874) and as **Supplementary Software**) has a precision of  $\sim 2$  nm in the  $x$  and  $y$  directions and  $\sim 5$  nm in  $z$  (at 50 Hz), as determined from the s.d. of traces of immobilized microspheres (Online Methods and **Supplementary Fig. 1**). We corrected for mechanical drift by tracking the displacement of an immobilized reference microsphere attached to the surface (**Fig. 1a, iii**). Bright-field illumination was provided in epiconfiguration, through the objective. The light was reflected by an aluminum layer sputtered on top of the flow cell, below the opaque piezo element. This allowed for a simple, compact design compatible with a standard microscope with epi-illumination (**Supplementary Fig. 2**).

<sup>1</sup>Department of Physics and Astronomy, VU University Amsterdam, Amsterdam, the Netherlands. <sup>2</sup>LaserLaB Amsterdam, VU University Amsterdam, Amsterdam, the Netherlands. <sup>3</sup>Division for Biomedical Physics, Innsbruck Medical University, Innsbruck, Austria. <sup>4</sup>These authors contributed equally to this work. <sup>5</sup>These authors jointly directed this work. Correspondence should be addressed to G.J.L.W. ([g.j.l.wuite@vu.nl](mailto:g.j.l.wuite@vu.nl)).

**Figure 1** | Principle of acoustic force spectroscopy. **(a, i)** The acoustic force device is integrated in a flow cell, and objects are imaged using an inverted microscope with objective lens (OL), digital camera (complementary metal-oxide semiconductor, CMOS), LED light source (455 nm) and 50/50 beam splitter (BS). **(a, ii)** The flow cell consists of two glass plates with a fluid chamber in between. An acoustic wave-generating piezo plate is attached to the upper glass slide, which has a sputtered mirroring aluminum layer for illumination. **(a, iii)** A single DNA molecule, attached at one end to the upper glass plate (black stars) and at the other to a microsphere, is stretched by acoustic forces acting on the microsphere. **(b)** Digital camera image of a DNA-tethered polystyrene microsphere (4.5- $\mu\text{m}$  diameter; DNA length, 8.4 kbp) and a silica reference microsphere (1.5- $\mu\text{m}$  diameter). Scale bar, 5  $\mu\text{m}$ . **(c)** Theoretically predicted acoustic energy ( $E_{ac}$ ) of the AFS device driven with a peak-to-peak voltage ( $V_{pp}$ ) of 5 V. **(d,e)** Predicted acoustic (Ac.) pressure distribution at 6.8-MHz **(d)** and 9.2-MHz **(e)** resonance frequencies across the glass and fluid layers. **(f)** Predicted forces for a 4.5- $\mu\text{m}$ -diameter polystyrene microsphere directed along the  $z$  direction (0.5-W input power). Microspheres near the upper surface ( $z = 0$ ) experience a force directed away from the surface at 6.8-MHz resonance and toward the surface at 9.2 MHz.



To validate our approach, we applied acoustic forces to stretch individual dsDNA tethers (8.4 kbp,  $\sim 2.8\text{-}\mu\text{m}$  contour length) attached at one end to the flow-cell surface and at the other end to a polystyrene microsphere (diameter, 4.5  $\mu\text{m}$ ) (Fig. 2a). Without driving the piezo, we observed diffusive motion of the tethered microsphere comparable to results of a tethered-particle motion experiment<sup>14</sup>. Driving the piezo at 9.0-MHz resonance pushed the microspheres toward the surface, allowing us to determine the zero at the  $z$  position. Operating at 6.7-MHz resonance pulled the microspheres away from the surface, quenching the Brownian motion of the microspheres in directions parallel to the surface because of the increased tension on the DNA tether.

To quantify DNA tension, we calculated the power spectrum of the microsphere position fluctuations (in the directions parallel to the glass interface) and fitted it with a model, using the tension as a free fit parameter (Online Methods and Fig. 2b). The planar nature of the acoustic waves allowed for the homogeneous application of forces over an area of several square millimeters (Supplementary Fig. 3). As predicted by equation (1), tension scaled with the volume of the particle (Fig. 2c) and was higher for silica than for polystyrene microspheres owing to silica's higher stiffness and density. In further agreement with theory, tension on the DNA tether scaled with the square

of the applied voltage (Fig. 2c), allowing for accurate control of tension with the piezo-driving voltage.

Although acoustic forces acting on the microsphere can be changed rapidly, the speed of the tension response is limited by the effect of solvent drag on microsphere motion. For the microsphere sizes we tested, response time was  $< 1$  ms in the enthalpic force regime (i.e., at forces above  $\sim 1$  pN; Online Methods). Theory predicts that AFS precision is ultimately limited by thermal fluctuations, which we verified experimentally by determining the s.d. ( $\sigma_L$ ) of microsphere positions (Fig. 2d and Online Methods). Finally, AFS is very stable and thus allowed forces and positions to be measured over extended periods. Measurements of the length of a DNA molecule subjected to a 9-pN force showed no substantial drift over 16 h (Supplementary Fig. 4).

To demonstrate the use of AFS with a range of forces relevant to biomolecules, we performed experiments on individual dsDNA molecules (Fig. 3a). AFS allowed us to accurately determine the force-extension behavior of both torsionally unconstrained (8.4 kbp, 2.8- $\mu\text{m}$  contour length) and torsionally constrained DNA (10.1 kbp, 3.4- $\mu\text{m}$  contour length) over the full range of forces for which the double helix remains intact (0–65 pN and 0–110 pN for torsionally unconstrained and constrained DNA, respectively<sup>9,10</sup>). These experimental curves were well described by the extensible worm-like chain model<sup>15</sup>.

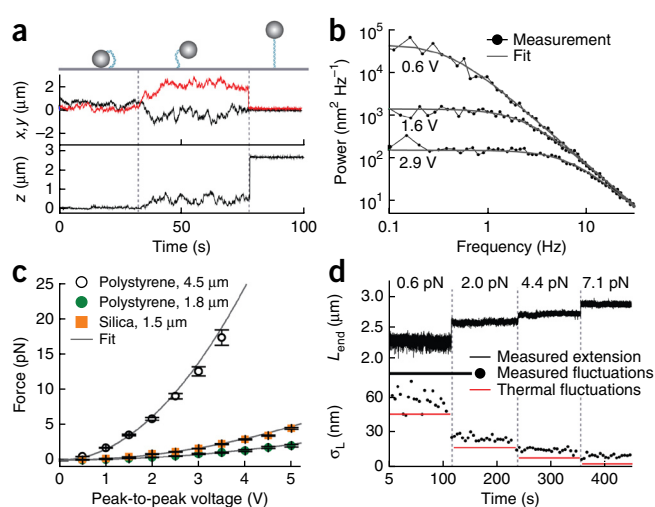
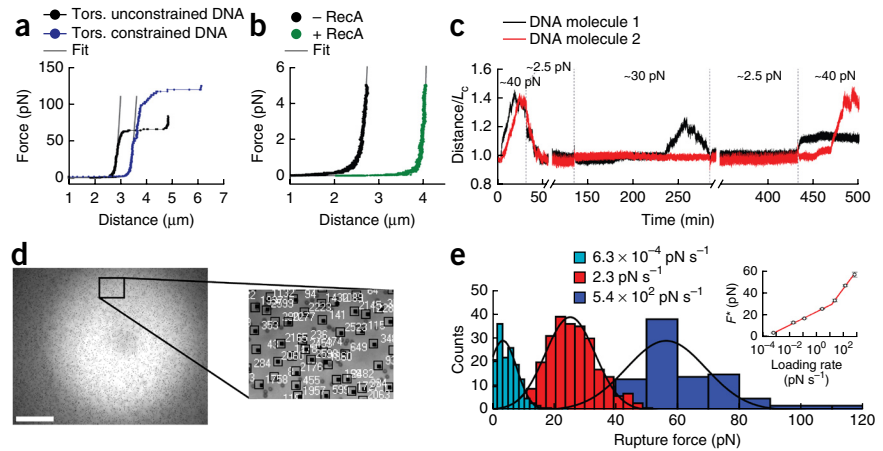


**Figure 2** | AFS applied to tethered DNA. **(a)** Time traces showing the  $x$  (black) and  $y$  (red) position of a DNA-tethered microsphere (polystyrene, diameter, 4.5  $\mu\text{m}$ ; DNA length, 8.4 kbp). In the first 35 s, the piezo was driven at 9.0 MHz (peak-to-peak voltage ( $V_{pp}$ ) = 0.5 V), pushing the microsphere toward the surface. From 35–80 s, no acoustic force was applied, and after 80 s the piezo was driven at 6.7 MHz ( $V_{pp}$  = 2.4 V), pulling the microsphere away from the surface. **(b)** Measured and fitted mean power-spectra values of the microsphere's  $x$  and  $y$  positions using a Lorentzian function (Online Methods). Forces obtained were  $0.61 \pm 0.07$ ,  $3.9 \pm 0.1$  and  $11.8 \pm 0.2$  pN (fit value  $\pm$  s.d.) at  $V_{pp}$  = 0.6, 1.6 and 2.9 V piezo-driving voltages, respectively (piezo driven at 6.7 MHz). **(c)** Forces acting on polystyrene and silica microspheres tethered to the glass surface with DNA (length, 8.4 kbp) as determined from power-spectrum analysis (data are mean  $\pm$  s.e.m.,  $n = 30$ ). Quadratic fits yielded quadratic constants of  $1.54 \pm 0.06$ ,  $0.19 \pm 0.01$ ,  $0.089 \pm 0.003$  pN  $\text{V}^{-2}$  (fit value  $\pm$  s.d.) for the 4.5-, 1.5- and 1.8- $\mu\text{m}$  microspheres, respectively. **(d)** Noise characterization of the measured end-to-end distance ( $L_{end}$ ). Top,  $L_{end}$  as a function of time (acquired at 50 Hz) for different forces. Bottom, s.d. ( $\sigma_L$ ) of the measured length fluctuations and calculated thermal fluctuations (Online Methods).

**Figure 3** | Force-extension, constant-force and dynamic force spectroscopy measurements.

(a) Stretching curve of 8.4-kbp torsionally (Tors.) unconstrained DNA and 10.1-kbp torsionally constrained DNA and their corresponding extensible worm-like chain fits (8.4-kbp DNA: persistence length, 52 nm; contour length, 2.87  $\mu\text{m}$ ; stretch modulus, 2,000 pN; 10.1-kbp DNA: persistence length, 50 nm; contour length, 3.46  $\mu\text{m}$ ; stretch modulus, 2,100 pN). (b) Experimental force-extension curves of an 8.4-kbp DNA molecule measured in the absence or presence of 1  $\mu\text{M}$  RecA (pH 6.4). Fits yielded contour lengths of  $2.82 \pm 0.02 \mu\text{m}$  and  $4.26 \pm 0.04 \mu\text{m}$  (fit value  $\pm$  s.d.) for bare DNA and RecA-coated DNA, respectively. (c) Normalized length-time traces of two DNA molecules (8.4 kbp) in the presence of 0.5  $\mu\text{M}$  RecA (pH 7.4): DNA length increased at 40 pN and decreased at 2.5 pN. At 30 pN, stochastic length variations were observed. (d) Typical field of view (scale bar, 200  $\mu\text{m}$ ) of the dynamic force spectroscopy measurements, showing thousands of microspheres (diameter, 2.8  $\mu\text{m}$ ). The majority of these were tracked in real time. Zoom shows an area with several regions of interest (black squares) around tracked microspheres (black points) and the identification number given by the tracking software. (e) Rupture-force distribution of the Dig::anti-Dig bond at different loading rates. Each histogram of rupture counts was obtained from a single field of view. Inset, most probable rupture force ( $F^*$ ), obtained from the Gaussian fits, as a function of loading rate. Error bars, s.e.m.;  $n = 145$ .



Next, we used AFS to investigate how protein binding affects DNA mechanical properties by probing RecA filament assembly on torsionally unconstrained dsDNA (8.4 kbp) in the presence of ATP. A single RecA protein binds to 3 bp and increases their contour length by 0.51 nm (ref. 16). A dsDNA molecule completely coated with RecA thus has a contour length 1.5-fold longer than that of naked DNA. Such an increase could be clearly resolved in force-extension measurements using AFS (Fig. 3b).

To obtain insight into the dynamics and stochasticity of cooperative RecA binding to DNA, we used AFS to perform constant-force measurements of the extension of multiple DNA molecules simultaneously in the presence of RecA and ATP. It is well documented that RecA binding to dsDNA depends strongly on DNA tension: the binding rate increases with tension, whereas the unbinding rate decreases<sup>17</sup>. Monitoring of DNA extension showed that, indeed, RecA-filament formation was enhanced at a tension of 40 pN, leading to an effective increase in DNA length (Fig. 3c). RecA-filament disassembly was dominant at 2.5 pN, resulting in shortening of the DNA molecule. At an intermediate tension of 30 pN, competition between filament formation and disassembly led to heterogeneity between two DNA tethers: one increasing length owing to filament growth after a rare nucleation event, followed by a period of decrease due to disassembly, the other showing no change.

Finally, to demonstrate the massive multiplexing capability of AFS, we used dynamic force spectroscopy to unravel the energy landscape of the digoxigenin (Dig)::anti-Dig antigen-antibody interaction. We tracked over 2,000 microspheres in real time in  $x$  and  $y$  within one field of view (Fig. 3d). We applied very strict selection criteria to discriminate singly tethered from doubly tethered and surface-attached microspheres, yielding approximately 8% (~150) singly Dig::anti-Dig-tethered spheres (using a 1.1-kbp DNA linker) in a typical field of view. Force calibration was performed independently for each of these spheres (Online Methods and Supplementary Figs. 5 and 6). When we used the tracking software, a single run of the machine yielded a complete bond-ruptures force histogram (Supplementary Software).

We performed measurements at seven loading rates spanning six orders of magnitude (from  $6.3 \times 10^{-4} \text{ pN s}^{-1}$  to  $5.4 \times 10^2 \text{ pN s}^{-1}$ ; Fig. 3e). Note that even higher loading rates are attainable when a camera with a higher frame rate is used. A plot of the rupture force against the logarithm of the loading rate showed two distinct linear regimes (Fig. 3e) that correspond to two energy barriers along the unbinding pathway<sup>18</sup>. Linear fits yielded a dissociation rate at zero force of  $k_{\text{off}1} = (7 \pm 1) \times 10^{-5} \text{ s}^{-1}$  (fit value  $\pm$  s.d. given throughout) and a distance from the ground state to the energy barrier of  $\Delta x_1 = 1.54 \pm 0.07 \text{ nm}$  at low loading rates; for high loading rates these values were  $k_{\text{off}2} = (2.7 \pm 0.7) \times 10^{-2} \text{ s}^{-1}$  and  $\Delta x_2 = 0.57 \pm 0.05 \text{ nm}$  (Online Methods). Previous single-molecule studies have yielded higher off-rates for Dig::anti-Dig bonds, indicating weaker binding<sup>7,19</sup>, which is most likely because of the different antibodies used<sup>20</sup> (Online Methods). Most dynamic force spectroscopy experiments to date have been performed using atomic force microscopy (AFM), which requires that individual bonds be broken one at a time. When we used the slowest loading ramp ( $6.3 \times 10^{-4} \text{ pN s}^{-1}$ ), it took on average several hours for a single bond to rupture. Consequently, measuring a histogram consisting of ~150 rupture events with this loading rate using AFM would take several months, which makes this regime difficult to access for AFM measurements.

AFS is an accurate single-molecule technique that provides insight into protein-DNA and protein-protein interactions by force-extension, constant-force and dynamic force spectroscopy measurements and can readily be extended to studies of other molecules and molecular interactions. Moreover, AFS is a unique single-molecule tool that combines a high-dynamic force range with massive multiplexing capabilities. Also taking into account its relative simplicity, low cost and compactness, which allow straightforward implementation in lab-on-a-chip devices, we anticipate that AFS will help to spread single-molecule methods from the realm of fundamental research in specialized laboratories toward more widespread application in areas such as molecular biology and medical diagnostics.

## METHODS

Methods and any associated references are available in the [online version of the paper](#).

Note: Any Supplementary Information and Source Data files are available in the [online version of the paper](#).

## ACKNOWLEDGMENTS

We thank A.S. Biebricher, T.P. Hoekstra and S. d'Haene for biochemical help; R.J. Limburg and P.J.M. Caspers for technical support; N. Laurens for his work on the tracking software; O.D. Broekmans for his help with making the software available online; M. Hill and P. Glynne-Jones (University of Southampton) for providing the software comprising the one-dimensional acoustical model; and D.D. Dunlap (Emory University) for supplying the torsionally constrained DNA construct. This work is part of the research program of the Foundation for Fundamental Research on Matter (FOM) (E.J.G.P. and G.J.L.W.), which is part of the Netherlands Organization for Scientific Research (NWO). We acknowledge support by NWO VICI (E.J.G.P. and G.J.L.W.) as well as a European Research Council (ERC) starting grant (G.J.L.W.) and an ERC advanced grant (M.R.-M.).

## AUTHOR CONTRIBUTIONS

G.S., G.J.L.W. and E.J.G.P. initiated the development of acoustic force spectroscopy as a novel single-molecule technique rooted in discussions during a visit to the laboratory of G.T. and M.R.-M. G.T. and M.R.-M. provided the background knowledge and know-how on acoustic forces. G.S. conceived of and designed the instrument and research. G.S. and D.K. built the instrument, wrote the software, performed the experiments and analyzed the data. G.T., E.J.G.P. and G.J.L.W. advised on instrument design. E.J.G.P. and G.J.L.W. supervised the project. G.S., D.K., G.T., M.R.-M., E.J.G.P. and G.J.L.W. wrote the paper.

## COMPETING FINANCIAL INTERESTS

The authors declare no competing financial interests.

Reprints and permissions information is available online at <http://www.nature.com/reprints/index.html>.

1. Bustamante, C., Cheng, W. & Meija, Y.X. *Cell* **144**, 480–497 (2011).
2. Neuman, K.C. & Nagy, A. *Nat. Methods* **5**, 491–505 (2008).
3. Herbert, K.M., Greenleaf, W.J. & Block, S.M. *Annu. Rev. Biochem.* **77**, 149–176 (2008).
4. Zhao, Y. *et al. Lab Chip* **13**, 2183–2198 (2013).
5. De Vlaminck, I. & Dekker, C. *Annu. Rev. Biophys.* **41**, 453–472 (2012).
6. Kim, S., Blainey, P.C., Schroeder, C.M. & Xie, X.S. *Nat. Methods* **4**, 397–399 (2007).
7. Halvorsen, K. & Wong, W.P. *Biophys. J.* **98**, L53–L55 (2010).
8. Fazio, T., Visnapuu, M.-L., Wind, S. & Greene, E.C. *Langmuir* **24**, 10524–10531 (2008).
9. Smith, S.B., Cui, Y. & Bustamante, C. *Science* **271**, 795–799 (1996).
10. van Mameren, J. *et al. Proc. Natl. Acad. Sci. USA* **106**, 18231–18236 (2009).
11. Settnes, M. & Bruus, H. *Phys. Rev. E* **85**, 016327 (2012).
12. Heller, I. *et al. Nat. Methods* **10**, 910–916 (2013).
13. Glynne-Jones, P., Boltryk, R.J. & Hill, M. *Lab Chip* **12**, 1417–1426 (2012).
14. Laurens, N. *et al. Nucleic Acids Res.* **37**, 5454–5464 (2009).
15. Odijk, T. *Macromolecules* **28**, 7016–7018 (1995).
16. Chen, Z., Yang, H. & Pavletich, N.P. *Nature* **453**, 489–494 (2008).
17. Fu, H., Le, S., Muniyappa, K. & Yan, J. *PLoS ONE* **8**, e66712 (2013).
18. Merkel, R., Nassoy, P., Leung, A., Ritchie, K. & Evans, E. *Nature* **397**, 50–53 (1999).
19. Neuert, G., Albrecht, C., Pamir, E. & Gaub, H.E. *FEBS Lett.* **580**, 505–509 (2006).
20. Moayed, F., Mashaghi, A. & Tans, S.J. *PLoS ONE* **8**, e54440 (2013).

## ONLINE METHODS

**Experimental setup.** For the force-extension and constant-force measurements (Figs. 1 and 2a–c), a 40× microscope objective was used to image and illuminate the tethered microspheres, together with automatic focus-drift correction (Nikon, Perfect Focus, CFI Plan Fluor 40×, NA 0.75). Images were taken with a CMOS camera (Thorlabs, DCC1545M). For the dynamic force spectroscopy measurements (Fig. 3d,e) a 10× microscope objective (Nikon, CFI Plan Fluor 10×, NA 0.30) was used in combination with a 0.45× c-mount adaptor (Nikon, MQD42040). Images were obtained with a CMOS camera (Thorlabs, DCC3240M, with a full-frame frame rate of 60 Hz). For illumination, a fiber-coupled blue LED (Thorlabs, M455F1) was coupled into the imaging path with a 50:50 beam-splitter plate (Thorlabs, EBS2). Reference images required for particle tracking in  $z$  were obtained by mounting the AFS device consisting of a flow chamber and a piezo plate. The borosilicate-glass flow chamber (Micronit Microfluidics B.V.) consisted of bottom and top glass plates of 170 μm and 1 mm thickness, respectively, the fluid channel width was 2 mm and thickness was 100 μm. On top of the flow cell, a thin (~200 nm) aluminum layer was applied, serving as a mirror allowing for bright-field microscopy in epiconfiguration. The disk-shaped piezo element (Meggit Sensing Systems, material PZ26) had a diameter of 7 mm and a thickness of 0.22 mm and was equipped with wrap-around gold-nickel (1.5–2 μm nickel and a few nanometers of gold) electrodes allowing connection of both electrodes from the same side. The piezo element was glued to the chamber with a cyanoacrylate adhesive (Permatex, 40150A) (Supplementary Fig. 2). The piezo element was driven with a function generator (Agilent, 33250A) in combination with an RF-amplifier (SCD, ARS 2\_30\_30, 50-Ω impedance, 10-W max. output power). A maximum driving voltage of 20 V (peak to peak,  $V_{pp}$ ) was applied, which did not result in ultrasonic cavitation. Powers used in our measurements did not lead to sample heating of more than a few degrees (Supplementary Fig. 7). When the piezo element was directly connected to the function generator, the maximum voltage that could be applied was  $V_{pp} = 4.0$  V (at 6.7 MHz). The thickness of the individual layers was not critical for the construction of an AFS device because tolerances were quite large (Supplementary Fig. 8). One important feature was the use of a thin layer of glue to attach the piezo element to the flow chamber<sup>13</sup>, which we achieved by applying force to the piezo plate while gluing.

**One-dimensional acoustical model.** To provide insight into the operation of the AFS device and for identifying acoustic resonances with the desired properties, we used a one-dimensional model, as previously described<sup>13,21</sup>. The model considers the different layers (piezo, glass and fluid) as analogous to a set of electrical transmission lines in which the voltage represents the acoustic pressure. The impedance of every layer is determined by the density and the speed of sound of the different layers. The piezo layer is driven by an applied voltage, which is coupled to mechanical quantities via a transformation ratio that is defined by the piezo material. When the thickness, impedance and damping of all layers are known, resonance frequencies, acoustic pressures and velocities along the different layers can be calculated. Our layered resonator was modeled with a transducer of PZT4D material (thickness  $T = 220$  μm, speed of sound  $c = 4,530$  m s<sup>-1</sup>, density

$\rho = 7,700$  kg m<sup>-3</sup>, piezo-constant  $h_{33} = 2.37 \times 10^9$  V m<sup>-1</sup>, relative permittivity  $\epsilon_r = 700$ ), and carrier ( $T = 1,000$  μm) and reflector ( $T = 170$  μm) layers of glass ( $c = 6,000$  m s<sup>-1</sup>,  $\rho = 2,200$  kg m<sup>-3</sup>) and water as the fluid ( $T = 100$  μm,  $c = 1,480$  m s<sup>-1</sup>,  $\rho = 1,000$  kg m<sup>-3</sup>). Forces were calculated for polystyrene particles ( $c = 1,960$  m s<sup>-1</sup>,  $\rho = 1,000$  kg m<sup>-3</sup>). The Quality ( $Q$ )-factor (ratio between the stored and dissipated acoustic energy) accounts for the damping and all other losses throughout the resonant device. These values are generally much lower than material  $Q$ -factors and are commonly determined experimentally<sup>22</sup>. We assumed  $Q = 230$  in every layer to match the calculated with the measured forces. The electrodes of the transducer and the glue layer were neglected in the acoustical model because of their relatively small thickness.

**Microsphere tracking.** Acquired images were processed in real time to extract the microsphere positions in three dimensions. To determine the  $x$  and  $y$  position, we applied a cross-correlation algorithm<sup>14</sup>, whereas for the  $z$  position, a look-up table (LUT) was used, which contained a library of radial profiles previously acquired as a function of microsphere  $z$  position<sup>23</sup>. The precision of  $x$ - and  $y$ -position determination was about 3 nm, and for  $z$ -position determination, it was about 5 nm, at an acquisition rate of 50 Hz (Supplementary Fig. 1). Tracking software is freely available ([http://figshare.com/articles/AFS\\_software/1195874](http://figshare.com/articles/AFS_software/1195874) and Supplementary Software).

**Force calibration.** Experimental power spectra were obtained for each microsphere and binned using equal-sized blocks on the frequency axis (having  $n$  points per block). These binned power spectra were fitted by a Lorentzian using importance-weighted least-squares<sup>24,25</sup>:

$$P(f) = \frac{D/(2\pi^2)}{f^2 + (k/(2\pi \times \gamma_{\text{fax}}))^2} \quad (2)$$

with  $D = k_B T / \gamma_{\text{fax}}$  as the microspheres' diffusion constant,  $\gamma_{\text{fax}}$  the effective drag coefficient,  $k_B$  Boltzmann's constant,  $T$  the temperature,  $f$  the frequency and  $k$  the stiffness of a Hookean spring acting on the microsphere in the  $x$  and  $y$  dimension,  $k = F / (L_{\text{ext}} + R)$ . In this expression of  $k$ ,  $F$  is the force,  $L_{\text{ext}}$  is the measured extension of the DNA and  $R$  is the radius of the microsphere. Because microsphere and surface were in close proximity, their hydrodynamic interaction was taken into account using Faxén's law to calculate the effective drag on the microsphere<sup>25</sup>. Both  $D$  and  $F$  were used as free fit parameters. The values for  $D$  obtained from the fits were bias corrected by  $D_{\text{cor}} = D \times (n / (n - 2))$  to account for the non-Gaussian-distributed data in each block<sup>26</sup>. We plotted the bias-corrected power spectra together with the log-binned experimental spectra (Fig. 2b). We did not correct for aliasing or motion blurring as these effects did not contribute substantially to the calibrations performed here (Supplementary Fig. 9).

**Response time.** When the acoustic force acting on a tethered microsphere is changed by altering the driving voltage, the tension acting on the molecule does not change immediately but is delayed owing to viscous drag. To estimate the system response

time, we used Newton's second law, neglecting inertia because of the low Reynolds number of the system:

$$F(t) - \gamma \dot{z}(t) - k_z z(t) = 0 \quad (3)$$

with  $\dot{z}$  as the time derivative of the position  $z$ ,  $\gamma$  the drag coefficient and  $k_z$  the stiffness of the Hookean spring acting on the microsphere when it is displaced by a distance  $z$  from its equilibrium position at  $z = 0$ . When the acoustic force  $F(t)$  is suddenly switched from  $F_1$  to  $F_2$  at  $t = 0$ , then the microsphere approaches its equilibrium position following:

$$z(t) = \frac{F_2}{k_z} \left( 1 - \frac{F_2 - F_1}{k_z} e^{-\frac{k_z t}{\gamma}} \right) \quad (4)$$

The response time of the system is thus of the order  $\gamma/k_z$ , which is  $\sim 0.4$  ms for a  $4.5\text{-}\mu\text{m}$  diameter microsphere, assuming a  $8.4\text{-kbp}$  DNA stretched within the enthalpic regime ( $k_{\text{DNA}} \approx 100 \text{ pN } \mu\text{m}^{-1}$ ). This is much longer than the switching time of the driving voltage (which is of the order of  $100$  ns) and the time it takes until the acoustic standing wave reaches its final amplitude ( $2Q/\omega_0 \approx 10 \mu\text{s}$ ). The response time can thus be reduced by increasing system stiffness (using shorter DNA) or decreasing microsphere drag (using smaller microspheres).

**Thermal fluctuations and instrumental uncertainty.** The tethered microspheres undergo Brownian motion, leading to fluctuations in DNA end-to-end length. The s.d. of these fluctuations are estimated to be<sup>5</sup>

$$\sigma_{\text{therm}} = \left[ \frac{2k_{\text{B}}T}{\pi k_{\text{DNA}}} \arctan \left( \frac{2\pi\gamma_{\text{fax}} f_s}{k_{\text{DNA}}} \right) \right]^{\frac{1}{2}} \quad (5)$$

with  $f_s$  as the sampling frequency. For a  $4.5\text{-}\mu\text{m}$  microsphere tethered by a DNA molecule with length  $8.4 \text{ kbp}$  and stretched with a force of  $8.0 \text{ pN}$ , position fluctuations with an s.d.  $\sigma_{\text{therm}} \approx 3 \text{ nm}$  are expected (sampling frequency  $50 \text{ Hz}$ ). We measured larger fluctuations  $\sigma_{\text{L}} \approx 10 \text{ nm}$ , indicating that the instrumental uncertainty lay around  $10 \text{ nm}$ . A major contribution to this uncertainty was the tracking uncertainty, which was  $5 \text{ nm}$  for immobilized microspheres (**Supplementary Fig. 1**) and which was most likely larger for tethered spheres owing to motion blurring.

**Dynamic force spectroscopy measurement.** Bond-rupture measurements were performed to characterize the force-dependent unbinding kinetics of digoxigenin (Dig) and its antibody (polyclonal anti-digoxigenin (anti-Dig) from sheep, Roche, Cat. No. 11 333 089 001). In the assay, DNA molecules ( $1,091 \text{ bp}$ ) labeled with a single Dig antigen at one end and a streptavidin at the other end were used, which were tethered between an anti-Dig-coated surface and to a  $2.85\text{-}\mu\text{m}$  streptavidin-coated microsphere. Since the Dig::anti-Dig bond is by far the weakest link, all rupture events could be safely assigned to these bonds (see **Supplementary Fig. 6**). Note that our experimental approach allowed us to perform such experiments for a few thousand microspheres in parallel. Evaluation of this large amount of measured position data to extract rupture forces was done in parallel as well. It was therefore not more time

consuming to analyze thousands of traces than to analyze a single trace, apart from the computation time (which was well below  $1 \text{ min}$ ). Analysis software is freely available ([http://figshare.com/articles/AFS\\_software/1195874](http://figshare.com/articles/AFS_software/1195874) and **Supplementary Software**). Tracking the positions of all microspheres individually enabled us to discriminate between single-tethered microspheres and stuck or multiple-tethered microspheres (**Supplementary Fig. 5**). Using a selection criterion based on the total amount of motion, both microspheres that were stuck to the glass or hindered in some way in their motion (low r.m.s.) and microspheres that were poorly tracked (high r.m.s. owing to tracking errors) were discarded. The amount of motion was quantified using r.m.s. motion of the microsphere in  $x$  and  $y$  over a period of more than  $15 \text{ min}$  (ref. 27):

$$\text{r.m.s.} = \sqrt{\left\langle (x - \bar{x})^2 + (y - \bar{y})^2 \right\rangle_t} \quad (6)$$

with  $\bar{x}$  and  $\bar{y}$  as the average positions over time  $t$ . In our experiments, microspheres with r.m.s. values below  $350 \text{ nm}$  and above  $550 \text{ nm}$  were discarded. Determination of the symmetry of motion allows for discrimination between microspheres tethered with single and multiple DNA molecules. Only single-tethered particles exhibit symmetrical motion around their anchor points. Motion symmetry was calculated using the covariance matrix<sup>27</sup>:

$$C = \begin{pmatrix} \sigma_{xx} & \sigma_{xy} \\ \sigma_{yx} & \sigma_{yy} \end{pmatrix} \quad (7)$$

with

$$\sigma_{xy} = \langle xy - \bar{x}\bar{y} \rangle_t \quad (8)$$

The eigenvalues ( $\lambda_1, \lambda_2$ ) of  $C$  are equal for a perfectly symmetric motion. We used  $s = \sqrt{(\lambda_{\text{max}}/\lambda_{\text{min}})} < 1.2$  as a threshold. Forcst on single-tethered microspheres were then calibrated by applying a low acoustic force for a few minutes and measuring the microsphere positions. Power spectra of the  $x$  and  $y$  motion were calculated and fitted for every individual microsphere. Finally, a linear force ramp was applied (because of the quadratic dependence of force on applied voltage, this corresponds to a voltage that increases like a square-root function). The voltage and corresponding force at which a bond rupture took place were determined from the frame at which a given microsphere left the region of interest. To determine this frame, we compared the measured region of interest to a template image made when the microsphere was present at the beginning of the measurement. This was done by setting the following threshold:

$$\Delta\text{Template} = \sum_{n=1}^{144} \sqrt{(I_{n,\text{measured}} - I_{n,\text{template}})^2} > 200 \quad (9)$$

With  $I_n$  the intensity of the  $n$ th closest pixel to the subpixel tracked center of the microsphere (**Supplementary Fig. 6**).

**Energy landscape of the antibody-antigen bond.** The lifetime due to thermal activation of a weak noncovalent bond decreases when subjected to a force. Applying a force tilts the energy landscape, effectively lowering energy barriers, decreasing the likelihood that the bond stays intact. The faster the force is increased, the less time the system has to overcome the energy barriers via

thermal fluctuations. Therefore, the most probable rupture force of a population of bonds will increase as a function of loading rate. Linear regimes that appear over multiple orders of magnitude of loading rates can be interpreted as distinct energy barriers along the unbinding pathway<sup>18</sup>. For the Dig::anti-Dig bond, two regimes were observed, which we associate with two barriers. Parameters of these barriers were obtained by fitting the linear regimes with<sup>19</sup>

$$F^* = \frac{k_B T}{\Delta x} \ln \frac{r \Delta x}{k_B T \times k_{\text{off}}} \quad (10)$$

where  $\Delta x$  is the distance between the bound and the transition state,  $k_{\text{off}}$  is the dissociation constant at zero force and  $r$  is the loading rate.

**DNA tethers.** Both torsionally unconstrained (8.4 kbp) and constrained (10.1 kbp) DNA tethers were used. The 8.4-kbp DNA was obtained from a pKYBI vector that was restricted with KpnI and EcoRI (Fermentas), resulting in an 8,364-bp fragment. To the 3'-end overhang, a 29-mer (5'-C(T-Dig)CTC(T-Dig)CTCTC (T-Dig)TC TC(T-Dig)CTT CTC TT GTAC-3') was ligated. The 5'-end overhang was filled in using Klenow exo- polymerase (Fermentas) using biotin-14-dATP (Invitrogen) and dTTP (Fermentas), resulting in a DNA construct labeled with biotins on one end and digoxigenins on the other, on the same strand. The 10-kbp torsionally constrained DNA (gift of D. Dunlap) was based on pWM530 and was generated by doubling the length of an earlier construct to give a 11,564-bp sequence. Double-digesting with SpeI and ApaLI produced a fragment of 10,160 bp, which subsequently was ligated to ~1.4-kbp PCR fragments as tethers, containing either biotin or Dig<sup>28</sup>. For the bond-rupture measurements of Dig and anti-Dig, DNA (1,091 bp) with a single Dig label was used as described previously<sup>14</sup>. The DNA tethers were attached

to the surface using anti-Dig (Roche, Cat. No. 11 333 089 001). To this end, the flow cell was incubated for several minutes with an antibody-containing solution (20 µg/ml) for several minutes. Streptavidin-coated polystyrene (Spherotech) or silica microspheres (BaseClear) were attached to the other end of the DNA molecules.

**Buffers and RecA solutions.** Experiments on naked DNA were conducted in PBS (138 mM NaCl, 2.7 mM KCl and 10 mM phosphate (pH 7.4); Sigma) supplemented with 5 mM NaN<sub>3</sub> (sodium azide; Sigma), 0.5 mM EDTA (EDTA; Sigma) and 20 mg ml<sup>-1</sup> Casein (Sigma). To fully coat DNA with RecA (**Fig. 3b**), we used a 70 mM MES (pH 6.4) buffer (2-(*N*-Morpholino)ethanesulfonic acid; Sigma), with 1 µM RecA (New England BioLabs), 50 mM KCl, 10 mM MgCl<sub>2</sub>, 1 mM DTT (dithiothreitol; Sigma) and 1 mM ATP (Sigma). To analyze the binding and unbinding of RecA to DNA (**Fig. 3c**), we used a 70 mM Tris-HCl (pH 7.5) buffer, containing 0.5 µM RecA, 10 mM MgCl<sub>2</sub>, 5 mM DTT and 1 mM ATP.

**Sample-size justification.** For the different measurements in this study, we chose  $n$  large enough to avoid overlap of the error bars of subsequent data points.

21. Hill, M., Shen, Y. & Hawkes, J.J. *Ultrasonics* **40**, 385–392 (2002).
22. Hill, M., Townsend, R.J. & Harris, N.R. *Ultrasonics* **48**, 521–528 (2008).
23. Gosse, C. & Croquette, V. *Biophys. J.* **82**, 3314–3329 (2002).
24. te Velthuis, A.J.W., Kerssemakers, J.W.J., Lipfert, J. & Dekker, N.H. *Biophys. J.* **99**, 1292–1302 (2010).
25. Berg-Sørensen, K. & Flyvbjerg, H. *Rev. Sci. Instrum.* **75**, 594–612 (2004).
26. Nørrelykke, S.F. & Flyvbjerg, H. *Rev. Sci. Instrum.* **81**, 075103 (2010).
27. Han, L. *et al.* in *Mathematics of DNA Structure. Function and Interactions* (eds. Benham, C.J., Harvey, S., Olson, W.K., Sumners, D.W. & Swigon, D.) 123–138 (Springer, 2009).
28. Dunlap, D., Yokoyama, R. & Ling, H. *Nucleic Acids Res.* **40**, 11281–11291 (2012).